Chemical Engineering Science 122 (2015) 210–218

Contents lists available at ScienceDirect

Chemical Engineering Science

journal homepage: www.elsevier.com/locate/ces

A comparison of magnetic resonance, X-ray and positron emission particle tracking measurements of a single jet of gas entering a bed of particles

M. Pore [a], G.H. Ong [a], C.M. Boyce [a], M. Materazzi [b], J. Gargiuli [c], T. Leadbeater [c], A.J. Sederman [a], J.S. Dennis [a,*], D.J. Holland [a], A. Ingram [d], P. Lettieri [b], D.J. Parker [c]

[a] Department of Chemical Engineering and Biotechnology, University of Cambridge, New Museums Site, Pembroke Street, Cambridge CB2 3RA, UK
[b] Department of Chemical Engineering, University College London, Torrington Place, London WC1E 7JE, UK
[c] School of Physics and Astronomy, University of Birmingham, Edgbaston, Birmingham B15 2TT, UK
[d] School of Chemical Engineering, University of Birmingham, Edgbaston, Birmingham B15 2TT, UK

HIGHLIGHTS

- Magnetic resonance, PEPT and X-ray radiography were used complementarily.
- Length of jet of gas entering bed of Group B particles via 2 mm id orifice measured.
- Lengths were in good agreement for orifice velocities 50–100 m/s.
- Technique developed to use PEPT measurements to quantify jet length.

ARTICLE INFO

Article history:
Received 7 May 2014
Received in revised form
20 August 2014
Accepted 15 September 2014
Available online 28 September 2014

Keywords:
Imaging
Fluidization
Magnetic resonance
PEPT
X-ray
Particles

ABSTRACT

Measurements of the lengths of a single jet of gas entering a packed bed were made using magnetic resonance imaging (MRI), positron emission particle tracking (PEPT) and X-ray radiography and the results compared. The experiments were performed using a Perspex bed (50 mm i.d.) of poppy seeds: air at 298 K was admitted to the base of the bed through a single, central orifice, 2 mm in diameter. Poppy seeds (Geldart Group B, measured minimum fluidisation velocity with air at 298 K and 1 atm of 0.13 m/s and particle density $\sim$1060 kg/m^3) were used because of their high content of oil, which contains mobile protons and hence is suitable for MRI examination. The lengths of jet measured using the three techniques were in agreement between 50 m/s $< U_o <$ 100 m/s, where U_o is the superficial velocity through the orifice. Below U_o=50 m/s, X-ray measurements of jet lengths were shorter than those measured using MRI. This was attributed to the minimum diameter of void, found to be 5 mm, detectable in a 50 mm bed using ultra-fast X-ray measurements. PEPT is most commonly used to calculate particle velocities, whilst jet lengths are usually calculated from determinations of voidage. However, the particle locations determined in this work by PEPT were used to calculate a fractional occupancy count, from which a jet length could be inferred.

1. Introduction

Advances in measurement technologies and computing power have led to a new generation of non-invasive measurement techniques, such as Magnetic Resonance Imaging, X-ray Computed Tomography and Electrical Capacitance Tomography, to investigate gas–solid fluidisation. Ideally, a non-invasive measurement technique would be capable of measuring both voidage and velocities of particles to a high spatial and temporal resolution across a range of length scales in three-dimensional beds. However, no such technique currently exists with all these attributes, thus a range of methods is needed to investigate fluidisation phenomena. In order to use different methods reliably, they must be cross-validated to ensure that the same phenomena are seen identically. Here, three techniques were cross-validated: Magnetic Resonance Imaging (MRI), ultra-fast X-ray radiography and Positron Emission Particle

* Corresponding author. Tel.: +44 01223 334787.
E-mail address: jsd3@cam.ac.uk (J.S. Dennis).

http://dx.doi.org/10.1016/j.ces.2014.09.029

Tracking (PEPT). To reduce discrepancies arising from the experiment itself, the techniques were compared by imaging the same, temporally-stable system: a single, axisymmetric jet in a packed bed of Geldart Group B particles. This system is reproducible and gives the same jet shape and size when set up in different laboratories.

Previous investigations of jets in 3D beds have used pressure signal analysis (Vaccaro et al., 1997), optical probes (Wen et al., 1981, Blake et al., 1990), triboelectric probes (John et al., 1980; Berruti et al., 2009) and thermal tracer methods (Berruti et al., 2009, McMillan et al., 2005, Zhu et al., 2000). These methods are easy to use in large-scale, opaque industrial systems, but require the use of probes that distort the jet flow. X-ray radiography has been used to image beds non-invasively but early work was limited to projections through the bed which did not allow local values of properties to be calculated in 3D beds (Cleaver et al., 1995, Rowe et al., 1979). Magnetic resonance imaging (MRI) allows non-invasive imaging of gas–solid fluidised beds to a high spatial resolution, hence making it suitable for geometrical studies of jets (Müller et al., 2009). MRI is, generally, limited to measurements in small, non-metallic beds. However, the technique offers a new approach to studying, non-intrusively, the impact of walls on the behaviour of jets (Pore et al., 2012).

Much of the early work on jetting was conducted in 2D beds to allow visual measurement. However, when correlations from 2D and 3D beds (*e.g.* Blake et al. (1990), Müller et al. (2009) and Merry (1975)) are compared, those based on observations in 2D beds usually predict longer jet lengths than those from 3D beds. This suggests that the wall effects in 2D beds are significant and act to stabilise jets. Wen et al. (1981) also noted that longer jets were formed in 2D or semi-cylindrical beds compared to those in 3D beds, and therefore concluded that jet length correlations developed for 2D beds could not be applied to 3D systems. Even allowing for the difference between 2D and 3D, there remain large discrepancies amongst the correlations, arising from:

(1) The definition of a jet.
(2) The definitions of the geometrical parameters of jets.
(3) The experimental arrangement used.
(4) The measurement technique and method of data analysis used.

Jets have been defined in various ways. Thus, a jet could be (a) a permanent, temporally-stable void formed above the orifice (known as a permanent jet), or (b) a permanent region of high voidage above the orifice from which bubbles are formed and detach (known as a pulsating jet), or (c) a stream of bubbles formed at the orifice. As a result, the definitions of geometric parameters, such as jet length (L_j), jet diameter (D_j) and jet angle (θ), vary significantly between studies, *e.g.* those of Müller et al. (2009), Rees et al. (2006) and Cleaver et al. (1995). Various types of experimental arrangement have been used to measure jet phenomena, including a wide range of types of distributor, and with the bed held at various fluidising velocities.

Finally, the measurement technique and analysis of the subsequent results can also lead to discrepancies among studies. Early studies measured jet parameters using optical or probe measurements, which require relatively simple analysis of the raw results. Advances in computing and hardware have led to the use of tomographic techniques, which have the capability to image optically-opaque, three-dimensional systems non-invasively, unlike earlier optical and probe measurements. However, there is still potential for discrepancies between measurements using different imaging techniques, due either to the capability of the measurement technique itself or the reconstruction and analysis of images.

2. Experimental

2.1. Fluidised bed

Experiments were performed using a bed of poppy seeds fluidised with air at 298 K. Poppy seeds were used because of their high content of oil, which contains mobile protons and hence are suitable for MRI examination. The seeds had a diameter of 0.5 mm and particle density $\sim$1060 kg/m^3 (Geldart Group B) with a measured minimum fluidisation velocity (U_{mf}) with air at 298 K and 1 atm of 0.13 m/s. The height of the bed when slumped was constant at 115 mm. The bed was contained in a 50 mm i.d. Perspex (polymethyl methacrylate) column, fitted with a distributor with a single, central orifice of diameter 2 mm, (shown schematically in Fig. 1). The plenum chamber had a volume of $\sim$200 cm^3 to dampen fluctuations in gas pressure from the compressed air supply (regulated at 1 barg). The same apparatus was used to make measurements with all three imaging techniques.

The particles were loaded by pouring them into the empty bed with gas flowing at the minimum superficial velocity, U_{mf}, a technique found to improve the reproducibility of the experiments (Müller et al., 2009). Measurements were made for a succession of gas superficial velocities, U, starting at 0.30 m/s (corresponding to a velocity through the orifice, U_o=187 m/s) and progressively reduced to 0.04 m/s (U_o=23 m/s), allowing $\sim$100 s for the bed to stabilise after each reduction in the superficial gas velocity.

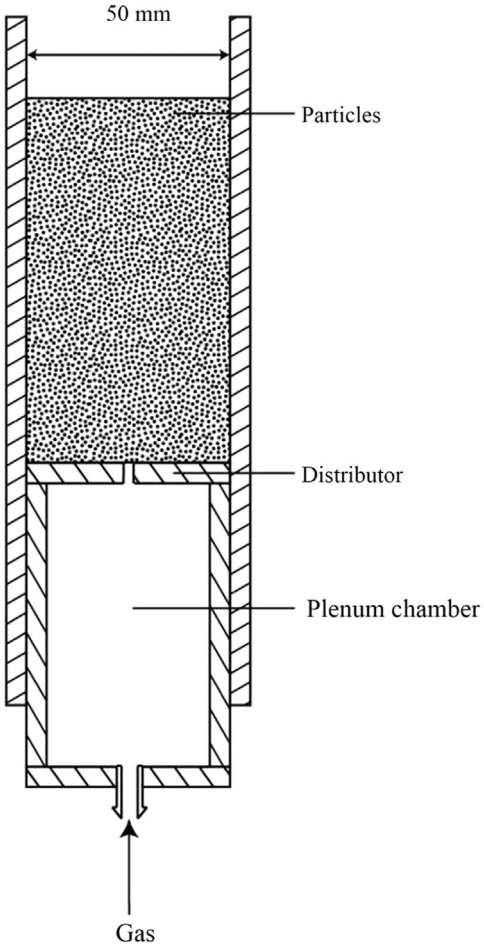

Fig. 1. Schematic diagram of the bed. The distributor contained a single, central orifice with an orifice diameter, d_o, of 2 mm.

2.2. Magnetic resonance imaging

A Bruker DMX200 spectrometer was used to image the particles, operating at a proton (^{1}H) frequency of 199.7 MHz with an actively shielded gradient system capable of producing a maximum gradient strength of 0.139 T/m. A birdcage radiofrequency (r.f.) coil of internal diameter 63 mm was used to excite and detect ^{1}H nuclei.

Multi-slice 2D spin echo imaging was used to produce time-averaged 3D images of the distributor region, similar to that described in (Rees et al., 2006). Images of two-dimensional slices (in the horizontal x–y plane) were acquired at 128×128 pixels with a field of view of 55 mm $\times$ 55 mm, giving an in-plane resolution of 0.43 mm. In the axial direction 41 slices, each 1 mm thick, were obtained, giving an axial resolution of 1 mm. Images were acquired with an echo time, T_E, of 2.51 ms, a recycle time, T_R, of 730 ms. Four scans were taken for each slice and images were time-averaged over $\sim$300 s.

2.3. Ultra-fast X-ray imaging

X-ray experiments were conducted using the high-power, pulsed X-ray system (developed by SPS Inspection Systems) at University College London (UCL). The X-ray source and detector were mounted so as to allow the object-to-intensifier distance (OID) and the source-to-intensifier distance (SID) to be varied. The apparatus uses a rotating anode, cooled by both air and oil, and the X-rays could be pulsed by pulsing the current to the cathode, achieving a minimum pulse length of 200 μs at a rate of 72 fps. The maximum current and voltage was 450 mA and 150 keV. The detector comprised a 300 mm $\times$ 300 mm image intensifier (with an imaging area of 270 mm $\times$ 270 mm) fitted with a caesium iodide scintillator coupled to a CCD camera with a resolution of 1040×1024 pixels. Selection of the best X-ray settings was made by varying the following five parameters: (a) focal spot size, (b) current, (c) voltage applied, (d) distance from source to bed and (e) distance from bed to intensifier. The maximum current available was used, whilst the voltage was restricted to prevent saturation of the receiver for higher flow rates. The parameters used in the present work are given in Table 1. The jet length reported was measured from three replicate experiments. The bed was emptied and refilled between measurements to minimise any hysteresis effects.

2.4. Positron emission particle tracking

Positron Emission Particle Tracking (PEPT) measurements were made at the University of Birmingham. A dual-headed gamma-camera (ADAC Laboratories, California, U.S.A) was used to detect coincident γ-ray emissions from the tracer particle containing the radionuclide F^{18}. The tracer particle was one of the poppy seeds, activated by immersing it in water containing positron-emitting fluorine18 followed by drying. It therefore had the same size and mass of the bulk material. The radionuclide emits a positron, which decelerates over a short distance before interacting with an electron. The positron and electron are annihilated and a pair of back-to-back 511 keV γ-rays is emitted, which can be used to locate the source of the annihilation. Each of the two detectors of the positron camera had an imaging area of 590 mm $\times$ 470 mm. The principle of γ-ray detection systems is similar to X-ray systems: the incoming radiation interacts with a scintillator to emit electrons. The signal (either optical or electrical) is amplified and displayed. The PEPT system at the University of Birmingham has two plate detectors, each being a single sodium iodide crystal. The crystal plates are optically coupled to photomultiplier tubes (55 tubes per plate). The signal from the photomultiplier tubes is used to detect the location of the interaction of a γ-ray with the sodium iodide crystal (Parker et al., 2002).

Table 1
Settings used at the X-ray facility at UCL.

Voltage	45 keV
Current	400 mA
Pulse length	0.2 ms
Frame rate	72 fps
Focal spot diameter	0.6 mm

If a single positron-emitting particle is present in a granular flow, theoretically it is possible to locate that particle by detecting only two sets of coincident gamma rays. In practice, approximately one hundred gamma ray pairs are required to locate the particle (Parker et al., 1993), but this number of detections occurs in a fraction of a second, making PEPT valuable when investigating fast-moving particles. The location algorithm used a set of coincident γ-ray emissions to determine the location of the tracer particle. Assuming the trajectories of the gamma rays are uncorrupted, for each detected pair of gamma rays there must be a point along the line between the two detection points (known as the line of response, LOR) at which the particle is located. This point will be the point at which the LOR for multiple γ-ray pairs intersect. However, γ-ray trajectories can be corrupted by a) Compton scattering of one or both γ-rays prior to detection, and, or b) by γ-rays emitted from the radionuclide in the tracer particle, but not due to the positron-electron annihilation. The algorithm was designed to discard corrupted trajectories (Parker et al., 1993). The algorithm requires four parameters, the values of which depend on tracer activity, tracer speed and the mass of material that must be penetrated by the photons. For each application these are selected on the basis of experience and trial and error. The parameters are:

Events per slice: this determines the number of photon pairs used to calculate each location. The selected value is a trade-off between temporal and spatial resolution (for slow moving tracers). In this case a value of 250 was selected.

Locations per slice: analogous to a moving average, this allows overlapping of data used for successive locations. A value of 5 was selected giving a five-fold increase in temporal resolution,

Fopt: this is the proportion of pairs that are retained after discarding the outliers. Low values give a tighter convergence and increased confidence in the location. A value of 0.2 was selected.

Maximum error: error is quantified as the spread of retained LORs around the final computed location, measured as the standard deviation of orthogonal distances. Selecting a maximum prevents very poor locations being used. A value of 5 mm was selected. In most applications, however, optimisation of the other parameters means that errors exceeding about 2 mm are unlikely.

With these parameters the temporal resolution was about 1 ms and spatial resolution (measured from observations of the stationary tracer) about 1 mm which is of the order of the size of the particle, 0.5 mm.

Each flow rate was imaged for approximately 30 min to ensure the tracked particle had traversed all of the fluidised regions of the bed. During the acquisition process, care was taken to ensure that the particle remained in motion throughout the acquisition. If the particle became stuck at any point during the experiment, the bed was emptied and the experiment restarted. For lower orifice velocities, the particle frequently became trapped and so it was not possible to obtain measurements below 45 m s^{-1} using PEPT. Jet lengths reported in this paper were based on an average of three jet length measurements, each taken from one third of the data set acquired over 30 min. The position vector was obtained in

Table 2
Summary of achievable resolutions, scales and capabilities of MRI, X-ray and PEPT used. References: (1) Holland et al. (2008a), (2) Holland et al. (2008b), (3) Müller et al. (2008), (4) Holland et al. (2010), (5) Lettieri and Yates (2013), (6) Ingram et al. (2007), (7) Yang et al. (2007), (8) Leadbeater et al. (2012) and (9) Wildman et al. (2012).

	MRI [1–4]	X-ray [5]	PEPT [6–9]
Temporal resolution (ms)	~1.5	~0.2	~1
Spatial resolution (mm)	~1	~0.1	~0.5
VELOCITY	Yes	No	Yes
dispersion	Yes	No	Yes
Granular temperature	Yes	No	Yes
Scale (bed dia.) (mm)	50	270	750

Cartesian coordinates and then converted to cylindrical polar coordinates in order to exploit the radial symmetry of the system.

A summary of the capabilities of the MRI, X-ray and PEPT imaging arrangements used in the present work is given in Table 2.

3. Image analysis

3.1. MRI

MR images were processed using the Rayleigh, noise-based thresholding method to produce a binary image of the jet void and the particulate phase. This is described in Supplementary Information, Section A, which also shows how jet lengths were accordingly calculated.

3.2. X-ray imaging

The quality of X-ray images was improved either by adjusting the experimental arrangement or during the post-processing of the images. Experimentally, the current and voltage used were adjusted to optimise the contrast and intensity of images. The focal spot size was chosen to be as small as possible to reduce geometric unsharpness effects. In addition, the SID and OID were minimised to reduce scattering of the X-ray beam. Beam hardening effects, S-distortion and veiling glare were found to be negligible here, presumably due to the relatively small size of the system studied. The first of these occurs because rays of longer path lengths are more heavily attenuated than those of shorter path length, due to both monochromatic attenuation and the scattering of low-energy photons. The shorter path length through the edges of a sample can, as a result, give rise to artificially bright edges, known as a beam hardening artefact. An 'S' distortion is caused by stray external magnetic fields, which can distort the path of photons and electrons within the intensifier, causing incorrect spatial registration on the X-ray image intensifier, and manifested when the lines in the image of a rectilinear square grid are S-shaped. Veiling glare is a blurring of the image occurring as a result of scattered X-rays at the input and output window of the X-ray image intensifier.

Post-processing of images was used to correct for non-uniform image intensity, pincushion distortion and magnification effects. In addition, the image resolution was decreased during post-processing in order to improve the signal-to-noise ratio. The sequence of operations to process images involved:

(1) Background correction.
(2) Magnification correction.
(3) Pincushion correction.
(4) Improvement of signal-to-noise ratio (SNR).
(5) Image thresholding.

Details of these corrections are given in Supplementary Information, Section B, with the whole being implemented in MATLAB®. Images were calibrated using images of a calibration grid, such as the grid shown in Fig. B3 in the Supplementary Information. An image of the grid was processed to correct for background intensity variation, magnification effects, pincushion distortion and resized to improve SNR. The resulting image was used to calculate the scaling of the X-ray image in terms of millimetres per pixel. Two grids were used: a wire mesh, with a grid spacing of 2 mm between wires, and a drilled grid of square pitch, with a spacing of 10 mm between orifices. The calibration was validated by calculating the spacing between orifices in an image of the drilled plate and was found to add an error of ± 1.1 mm to jet length measurements. This error is less than the resolution of the final, resized image and so did not adversely affect the measurements of the length of a jet.

The jet can be identified using image segmentation techniques, as with MRI. However, for X-ray imaging, the contrast and SNR are relatively low making the use of standard thresholding techniques challenging. In this research, two image segmentation approaches were used: (a) adaptive thresholding and (b) Canny edge detection (Canny, 1986). These are described in the Supplementary Information, Section B; however, in summary, the adaptive thresholding algorithm attempts to segment the image in an analogous manner to that used in the MRI analysis. The Canny edge detection algorithm identifies regions of the image with sharp changes in signal intensity. In both cases it was necessary to reduce the spatial resolution of the images from 0.26 to 1.28 mm/pixel in order to improve the SNR to a sufficient level to segment the image effectively.

3.3. PEPT

PEPT measurements consist of a series of times at which pairs of γ-rays are detected and the Cartesian coordinates of the location of the tracer particle at those times. PEPT has traditionally been used to calculate particle displacements, and hence velocities. However, in this research, fractional occupancy count was calculated from the PEPT measurements, *i.e.* the fraction of the total number of detections for the particle in a given voxel in order to compare the measurements with the X-ray and MRI measurements of the location of the jet. Imaging a jet with PEPT is challenging because there is only a small part of the bed in which the particle is moving and large regions where the particle remains static. In the method for determining fractional occupancy, firstly, the bed was split into cylindrical voxels of constant radial thickness, dr, and axial thickness, dz, of 2 mm, as shown schematically in Fig. 2. Each recorded γ-ray detection was assigned to the cylindrical voxel in which the particle was detected. The occupancy count for a given voxel, $n(r,z)$, was calculated as the number of times a particle was detected in a given voxel. Since the radial and axial thickness of the cylindrical voxels was kept constant, the volume of each voxel varied, and therefore the occupancy count was corrected by the volume of the voxel, to give an occupancy count per unit volume, n_v:

$$n_v(r,z) = \frac{n(r,z)}{\pi((r+dr)^2 - r^2)dz} \tag{1}$$

The fractional occupancy count for each voxel, N_v, was calculated as the fraction of the total number of particle detections measured during the experiment in the whole column, corrected by the volume of the voxel, thus:

$$N_v(r,z) = \frac{n_v(r,z)}{\sum_{r=0}^{D/2}\sum_{z=0}^{H} n(r,z)} \tag{2}$$

3.4. Using a characteristic parameter approach

Rayleigh, noise-based thresholding is robust, but requires prior knowledge of the signal intensity distribution and is not applicable to X-ray and PEPT measurements. Therefore, an alternative methodology for determining the jet heights was developed. Here, a profile of the signal intensity for MRI and X-ray measurements, and fractional occupancy count for PEPT measurements, along the centre line of the jet was calculated. In the case of MRI and X-ray measurements, the signal intensity is related to the voidage. In MRI, negligible signal is detected from the jet void and the signal intensity increases suddenly at the top of the jet because there is a high concentration of particles above the jet. Conversely, a high signal intensity is observed in the jet void in X-ray images because the beam is attenuated less as it passes through the jet void. Therefore, there is a sudden decrease in signal intensity at the top of the jet as the high concentration of particles above the jet causes increased attenuation of the X-ray beam. The signal intensity therefore serves as a "characteristic parameter" to distinguish between the location of a void and the location of the particles. The location of the boundary between these two regions can be identified by calculating the spatial derivative of the characteristic parameter as a function of position along the jet, an example of the classical edge detection problem in image analysis. It was hypothesised that an equivalent approach could be used to analyse PEPT measurements, when validated against measurements of voidage acquired using MRI and X-ray imaging. In this case, the characteristic parameter was chosen to be the fractional occupancy count, described in Section 3.3. A fast-moving particle in the jet void will have a low fractional occupancy count as it will spend only a short time in the jet region. As the particle enters the fluidised annulus, it will decelerate and hence the fractional occupancy count should increase suddenly at the top of the jet. The characteristic parameter method is compared with conventional image segmentation used with the MRI results, in Section 4 below.

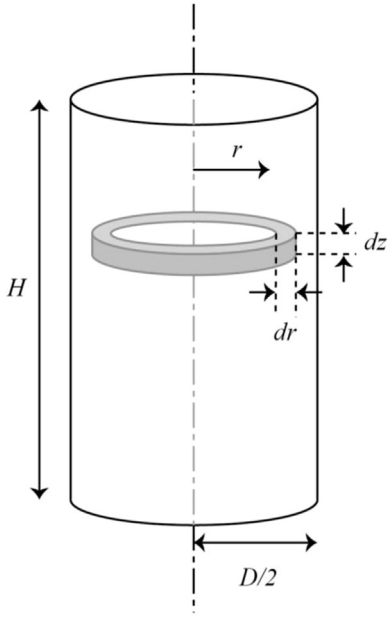

Fig. 2. A schematic diagram of the cylindrical voxels used for the calculation of fractional occupancy counts of the tracer particle in a fluidised bed of diameter D and height H.

4. Results

Three-dimensional maps of signal intensity were acquired using MRI. The jet length was calculated from the three-dimensional image using the noise-based thresholding method described in the Supplementary Information, Section A. A greyscale image of the central slice of the bed (slice thickness 0.4 mm) and the corresponding thresholded image of a jet formed at a superficial gas velocity $U=0.096$ m/s are given in Fig. 3(a) and (b). A greyscale X-ray image of a jet at the same flowrate is shown in Fig. 3(c). Qualitatively, it can be seen that there is good agreement between jet lengths for beds imaged using MRI and X-ray. A map of fractional occupancy counts, obtained from PEPT measurements in the vicinity of a jet, is given in Fig. 4, showing that low fractional occupancy counts are measured in the jet void.

A plot of signal intensities on the centre-line of the jet shown in Fig. 3(a) is given in Fig. 5(a). The first derivative of the signal intensity, calculated using the central difference method, is given in Fig. 5(b). The derivative was used to find the maximum gradient in the signal intensity plot, used to define as the height of the jet when using the characteristic parameter approach for MR images. Similar plots of centre-line signal intensities from X-ray images and fractional occupancy count from PEPT, and the corresponding plots of the first derivatives, are given in Figs.6 and 7, respectively.

In X-ray images, the signal intensity increases along the length of the jet as attenuation of the beam decreases with increasing diameter of the jet. Towards the top of the jet the signal intensity

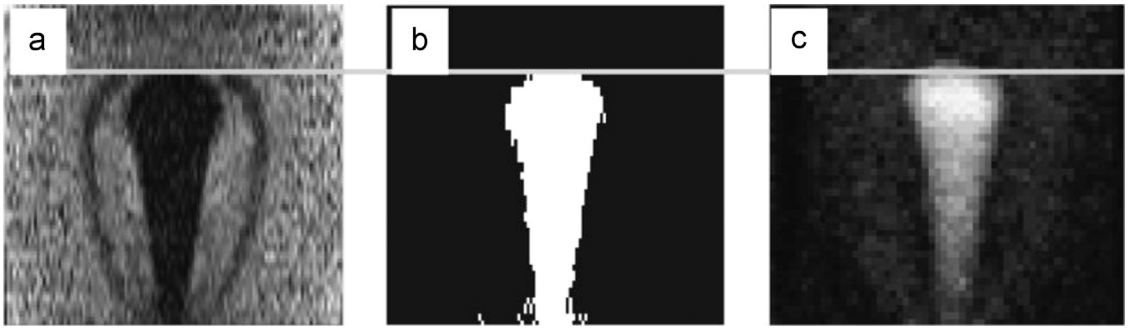

Fig. 3. Single jet in a packed bed of particles with a superficial gas velocity, $U=0.096$ m/s. (a) MR image of a centre slice (slice thickness of 0.4 mm) extracted from a series of stacked transverse images of the bed. (b) A thresholded image of the jet shown in (a) processed using the noise-based thresholding method. (c) A two-dimensional projection of the bed using X-ray imaging. The beam is attenuated by regions of high particle intensity, resulting in a low signal intensity corresponding to a low voidage. The dimensions of each image are 50 mm wide by 45 mm high.

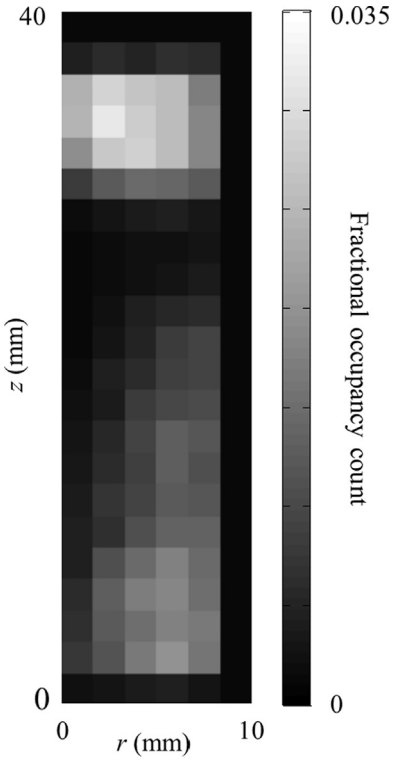

Fig. 4. Fractional occupancy counts measured along the length of the jet using PEPT measurements.

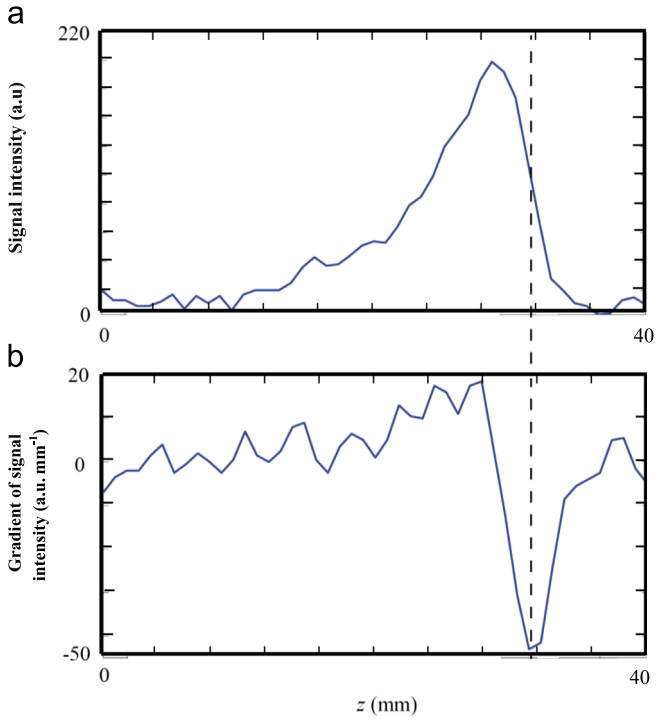

Fig. 6. (a) X-ray signal intensity along the centreline of the jet shown in Fig. 3(c) as a function of height, *z*, above the distributor. (b) The first derivative of the profile of the signal intensity in (a).

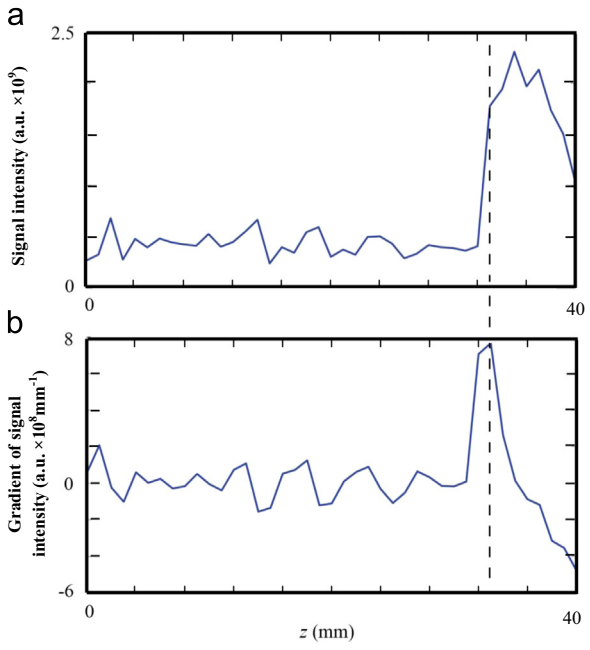

Fig. 5. (a) MR signal intensity along the centre-line of the jet shown in Fig. 3(a) as a function of height, *z*, above the distributor. (b) The first derivative of the profile of the signal intensity in (a).

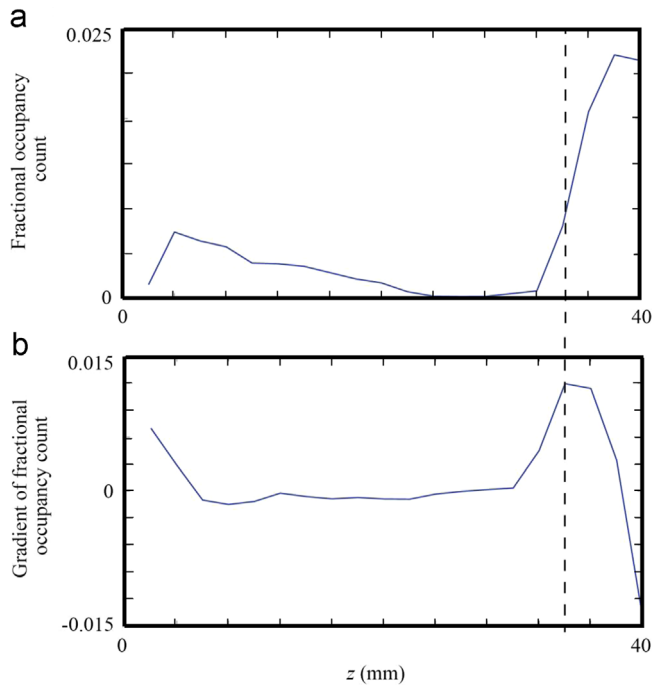

Fig. 7. (a) Fractional occupancy count along the centreline of the jet shown in Fig. 3 (a) as a function of height, *z*, above the distributor. (b) The first derivative of the profile of the signal intensity in a).

decreases as the projected length through the jet void decreases, leading to an increase in beam attenuation. The jet length was defined as the minimum of the derivative, *i.e.* the maximum negative gradient, associated with the increased signal attenuation at the top of the jet. Despite the noisy signal in the jet region, the sharp increase in the value of the first derivative was sufficiently large at all gas velocities to be easily detectable. The error due to partial volume effects (a maximum error of 8% of the jet length) was found to be greater than that due to noise (a maximum error of 3% of the jet length), indicating that the characteristic parameter approach is robust to noise.

For the PEPT measurements, the fractional occupancy count along the centre-line of the jet increases steeply at the top of the

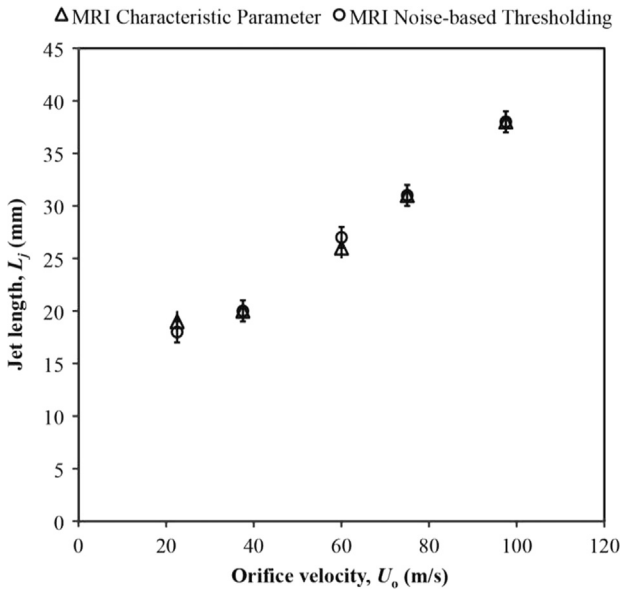

Fig. 8. A comparison of jet lengths measured using the Rayleigh noise-based thresholding method and the characteristic parameter approach applied to the same MR image.

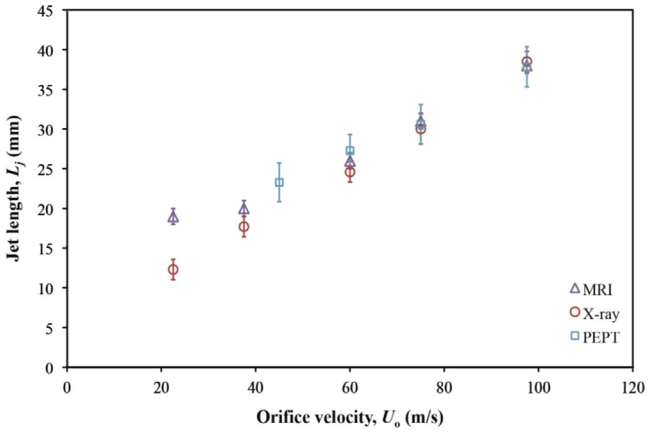

Fig. 9. A comparison of jet lengths measured using the characteristic parameter approach applied to MR and X-ray images of signal intensity, and occupancy times calculated from PEPT measurements.

jet, as seen in Fig. 4, and therefore the maximum of the first derivative can be used as a measure of the jet length.

Fig. 8 shows jet lengths measured using both noise-based thresholding and characteristic parameter methods for MR images at various superficial gas velocities. Good agreement is seen, despite noise-based thresholding being more rigorous than the empirical characteristic parameter approach. Errors in measurements for both methods of measuring jet length arose from partial volume effects.

Fig. 9 shows lengths of jet measured using the characteristic parameter approach applied to the MRI, X-ray and PEPT measurements. Errors for MRI measurements arise from partial volume effects. Errors for X-ray and PEPT measurements are also due to partial volume effects and were determined by the standard deviation of three measurements. Jet lengths measured using the three techniques at high flowrates ($U_o > 50$ m/s) are in good agreement. At low gas velocities ($U_o < 50$ m/s) jet lengths measured from X-ray images are lower than those measured using MRI.

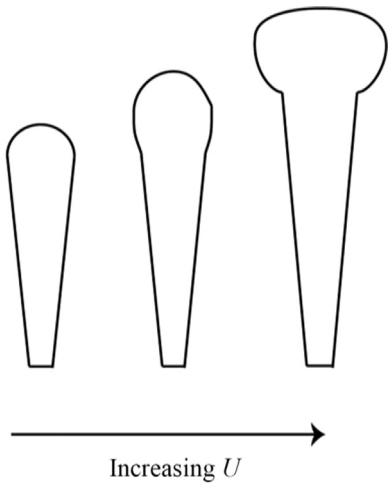

Fig. 10. A schematic diagram of the evolution of shapes of jets with increasing superficial gas velocity as observed using MRI and ultra-fast X-ray imaging.

5. Discussion

5.1. Jet shape using MRI and ultra-fast X-ray imaging

The signal from fast-moving particles in MR images might be attenuated as the particles pass out of a slice over the acquisition time or due to motion during an applied gradient in the magnetic field. For the pulse sequence used here, it is likely that the signals from particles travelling in excess of 0.7 m/s were attenuated. As a result, from the MR images alone it is unclear whether the shape of the jet seen is the actual shape of the void, or an image of only the slower-moving particles. Ultra-fast X-ray imaging on the other hand, captures a snap shot of the bed over an exposure time of 0.2 ms, thereby allowing any signal attenuation from fast-moving particles in the MR images to be identified. It was found that both MR and X-ray images qualitatively showed the same shapes. Thus, the shape of the jet was found to vary with increasing superficial gas velocity, as shown in Fig. 10. At low gas velocities, conical jets with hemispherical tops were formed. As the gas velocity was increased the top of the jet expanded, creating an elliptical dome on top of the conical jet stalk. The agreement between the X-ray and MRI jet shapes indicates that the MRI measurements were not adversely affected by the attenuation of the signals from rapidly-moving particles. It therefore appears that any loss of signal is restricted to particles located within the jet and therefore in this case attenuation of the signal owing to the fast motion of the particles simply leads to an increase in the contrast between particles in the low density, fast moving jet void and the slow moving, dense region surrounding the jet.

5.2. Inferring jet lengths from PEPT results

As noted earlier, fractional occupancy count is a suitable parameter for measuring jet length, a parameter usually associated with the voidage of the jet. One issue with analysing the jet length from PEPT in this manner is that the location of particles obtained from PEPT must be assigned to bins or voxels. The size of these bins can be chosen freely. Large bins will lead to a low noise level in the resulting image of fractional occupancy count, but a low spatial resolution. By contrast, small bins give a noisy fractional occupancy count but high spatial resolution. The accuracy of the measurement of the jet length will be determined by both the noise level and the spatial resolution. For any given bin size, the estimate of the jet length is characterised by an uncertainty of plus or minus half of that bin size. That is, the true height of the jet may

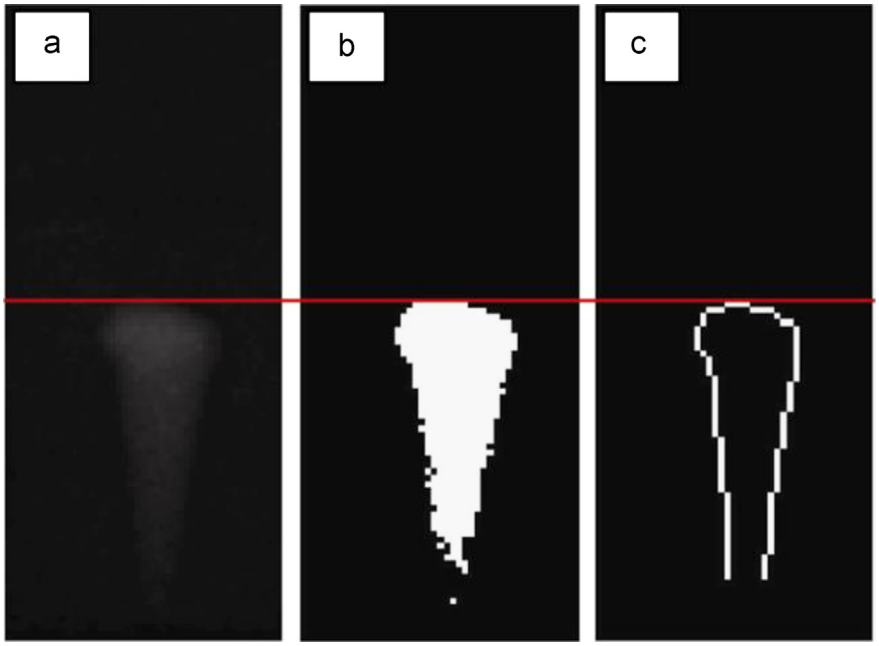

Fig. 11. X-ray images of a single jet formed at a formed from a single orifice distributor (orifice diameter, $d_o = 2$ mm) at a superficial gas velocity, $U = 0.16$ m/s showing (a) the greyscale image with improved signal-to-noise ratio, (b) a thresholded image and (c) the edges of the jet detected by Canny edge detection.

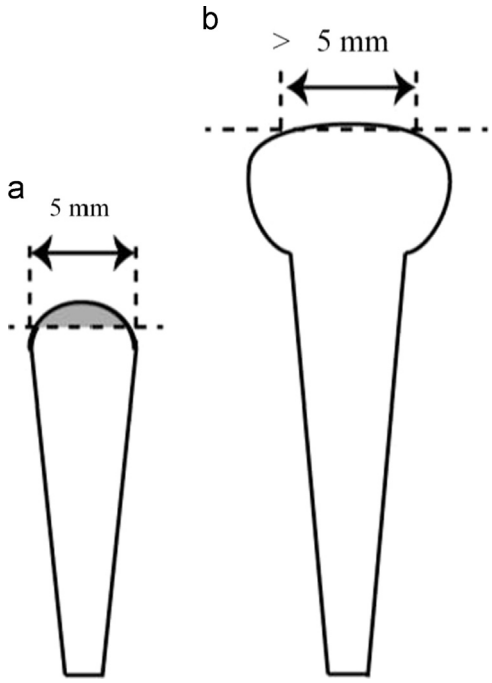

Fig. 12. Schematic diagram of a conical jet with a hemispherical cap produced at (a) low and (b) high velocities of gas through the orifice. Regions at the top of the jet with a projected diameter less than 5 mm (shaded in grey) will have insufficient contrast to be measured from X-ray images.

lie anywhere within a window of length equal to the bin size. In order to maximise the accuracy of the jet length calculation, jet lengths were estimated for a range of bin sizes. The jet length was determined by identifying the smallest bin size that located the top of the jet at the same position, to within the uncertainty defined by the size of the bin, as that estimated from larger bin sizes. In this way, any errors arising from the low SNR of the high spatial resolution data were minimised as the jet length from these measurements was only retained if it were consistent with the high SNR but low spatial resolution measurements obtained with large bins. The noise level can be decreased, and therefore the spatial resolution further increased, by acquiring data for a longer time, however this will not always be practicable.

5.3. Cross-validating jet length measurement methods

A simple method was used to measure jet lengths in order to compare the jet lengths measured using different imaging techniques. The characteristic parameter approach was compared to the more rigorous noise-based thresholding method. Good agreement was seen between the two methods, indicating that the characteristic parameter approach is accurate in measuring jet lengths from MR signal intensity images. It was therefore concluded that the characteristic parameter approach was also an effective method for analysing the X-ray and PEPT results.

5.4. Cross-validating measurements of jet lengths from MR, X-ray and PEPT images

Jet lengths measured using MRI and PEPT were in good agreement at the gas velocities investigated in this study. Measurements from X-ray images underpredicted jet lengths at low gas velocities by up to 5 mm, a discrepancy attributed to the minimum diameter of a void detectable with the ultra-fast X-ray equipment used.

Contrast in X-ray images is dependent on the degree of attenuation of the beam as it passes through regions of high and low voidage in the bed. If a region of high voidage is of a small diameter relative to the diameter of the fluidised bed, the beam will not be significantly attenuated, hence reducing the contrast and making the void indistinguishable from the dense phase. Fig. 11 compares qualitatively the value of jet heights measured using the adaptive thresholding and Canny edge detection methods. Good agreement is seen between the two methods. Fig. 11 also shows that the base of the single jet is not visible when the diameter of the jet is approximately 5 mm or smaller. The contrast in regions where the jet was small was limited by the x-ray power used. A higher power could be used on the x-ray but this would

increase the potential for burnout of the detector. Here it was decided to use the same x-ray power settings for all measurements, and therefore the maximum power was limited by the measurements with the highest orifice velocity.

Jets produced at low gas velocities were seen to be conical with hemispherical tops. Therefore regions at the tops of the jets with a diameter less than 5 mm will not be distinguishable using X-ray images, as shown schematically by the shaded area in Fig. 12a. At large gas velocities this does not occur because the tops of the jets are flattened ellipsoids and hence the projected diameter through the top of the jet is greater than 5 mm, as seen in Fig. 12b.

6. Conclusions

Measurements of lengths of a single gas jet in a packed bed at increasing superficial gas velocity, imaged using MRI, PEPT and X-ray radiography, were cross-validated. The jet lengths measured using the three techniques were in agreement using orifice velocities in the range $50\ \text{m/s} < U_o < 100\ \text{m/s}$ for the Geldart Group B particles used in the present work. Below 50 m/s, X-ray measurements of jet lengths were shorter than those measured using MR imaging. This was attributed to the minimum diameter of void that could be detected in a 50 mm bed using ultra-fast X-ray measurements, $\sim$5 mm.

PEPT is most commonly used to calculate particle velocities, whilst jet lengths are usually calculated from determinations of voidage. However, the particle locations determined in this work by PEPT were used to calculate a fractional occupancy count, from which a jet length could be inferred, a novel development.

Lengths of jets were determined with the three imaging modalities using identical experimental arrangements, a fixed definition of jet length and a characteristic parameter approach to analysing the results. Accordingly, any remaining discrepancies between lengths of jet measured by the various modalities could be attributed to the imaging techniques itself. Thus, the imaging techniques alone were cross-validated. It is clear that using multiple techniques to image a system gives more information about the fluidisation phenomena occurring than would be possible if each imaging technique were used alone.

Acknowledgements

Financial support from the EPSRC (Grant no. EP/F041772/1) and the Cambridge Philosophical Society (for MP) is gratefully acknowledged.

Appendix A. Supplementary information

Supplementary data associated with this article can be found in the online version at http://dx.doi.org/10.1016/j.ces.2014.09.029.

References

Berruti, F., Dawe, M., Briens, C., 2009. Study of gas–liquid jet boundaries in a gas–solid fluidized bed. Powder Technol. 192 (3), 250–259.

Blake, T.R., Webb, H., Sunderland, P.B., 1990. The nondimensionalization of equations describing fluidization with application to the correlation of jet penetration height. Chem. Eng. Sci. 45 (2), 365–371.

Canny, J., 1986. A computational approach to edge detection. IEEE Trans. Pattern Anal. Machine Intell. 8 (6), 679–698.

Cleaver, J.A.S., Ghadiri, M., Tuponogov, V.G., Yates, J.G., Cheesman, D.J., 1995. Measurement of jet angles in fluidized beds. Powder Technol. 85 (3), 221–226.

Holland, D., Müller, C., Sederman, A., Mantle, M., Gladden, L., Davidson, J., 2008a. Magnetic resonance imaging of fluidized beds: recent advances. Theor. Found. Chem. Eng.. 42 (5), 469–478.

Holland, D.J., Müller, C.R., Dennis, J.S., Gladden, L.F., Sederman, A.J., 2008b. Spatially resolved measurement of anisotropic granular temperature in gas-fluidized beds. Powder Technol. 182 (2), 171–181.

Holland, D.J., Müller, C.R., Dennis, J.S., Gladden, L.F., Davidson, J.F., 2010. Magnetic resonance studies of fluidization regimes. Ind. Eng. Chem. Res. 49 (12), 5891–5899.

Ingram, A., Hausard, M., Fan, X., Parker, D.J., Seville, J.P.K., Finn, N., Evans, M., 2007. Portable Positron Emission Particle Tracking (PEPT) for Industrial Use. In: Berruti, F., Bi, X., Pugsley, T. (Eds.), Fluidization XII. Engineering Conferences International, New York, pp. 497–504.

John, W., Reischl, G., Devor, W., 1980. Charge transfer to metal surfaces from bouncing aerosol particles. J. Aerosol Sci. 11 (2), 115–138.

Leadbeater, T.W., Parker, D.J., Gargiuli, J., 2012. Positron imaging systems for studying particulate, granular and multiphase flows. Particuology 10 (2), 146–153.

Lettieri, P., Yates, J.G., 2013. New generation X-ray imaging for multiphase systems. In: Fluidization XIV: From fundamentals to Products. Kuipers, J.A.M., Mudde, R. F., van Ommen, J.R., Deen, N.G. (Eds.), Engineering Conferences International. New York ⟨http://dc.engconfintl.org/fluidization_xiv/56⟩ (Accessed 20.01.14).

McMillan, J., Zhou, D., Ariyapadi, S., Briens, C., Berruti, F., Chan, E., 2005. Characterization of the contact between liquid spray droplets and particles in a fluidized bed. Ind. Eng. Chem. Res. 44 (14), 4931–4939.

Merry, J.M.D., 1975. Penetration of vertical jets into fluidized beds. AIChE J. 21, 507–510.

Müller, C.R., Holland, D.J., Sederman, A.J., Mantle, M.D., Gladden, L.F., Davidson, J.F., 2008. Magnetic resonance imaging of fluidized beds. Powder Technol. 183, 53–62.

Müller, C.R., Holland, D.J., Davidson, J.F., Dennis, J.S., Gladden, L.F., Hayhurst, A.N., Mantle, M.D., Sederman, A.J., 2009. Geometrical and hydrodynamical study of gas jets in packed and fluidized beds using magnetic resonance. Can. J. Chem. Eng. 87 (4), 517–525.

Parker, D.J., Broadbent, C.J., Fowles, P., Hawkesworth, M.R., McNeil, P., 1993. Positron emission particle tracking—a technique for studying flow within engineering equipment. Nucl. Instrum. Methods Phys. Res. Sect. A: Accel., Spectrom., Detect. Assoc. Equip. 326 (3), 592–607.

Parker, D., Forster, R., Fowles, P., Takhar, P., 2002. Positron emission particle tracking using the new Birmingham positron camera. Nucl. Instrum. Methods Phys. Res. Sect. A: Accel., Spectrom., Detect. Assoc. Equip. 477 (1–3), 540–545.

Pore, M., Chandrasekera, T.C., Holland, D.J., Wang, A., Wang, F., Marashdeh, Q., Mantle, M.D., Sederman, A.J., Fan, L.-S., Gladden, L.F., Dennis, J.S., 2012. Magnetic resonance studies of jets in a gas–solid fluidised bed. Particuology 10 (2), 161–169.

Rees, A.C., Davidson, J.F., Dennis, J.S., S Fennell, P., Gladden, L.F., Hayhurst, A.N., Mantle, M.D., Müller, C.R., Sederman, A.J., 2006. The nature of the flow just above the perforated plate distributor of a gas-fluidised bed, as imaged using magnetic resonance. Chem. Eng Sci. 61 (18), 6002–6015.

Rowe, P.N., MacGillivray, H.J., Cheesman, D.J., 1979. Gas discharge from an orifice into a gas fluidised bed. Trans. Inst. Chem. Eng. 57, 194–199.

Vaccaro, S., Musmarra, D., Petrecca, M., 1997. A technique for measurement of the jet penetration height in fluidized beds by pressure signal analysis. Powder Technol. 92 (3), 223–231.

Wen, C.Y., Deole, N.R., Chen, L.H., 1981. A study of jets in a three-dimensional gas fluidized bed. Powder Technol. 31 (2), 175–184.

Wildman, R.D., Hrenya, C.M., Huntley, J.M., Leadbeater, T., Parker, D.J., 2012. Experimental determination of temperature profiles in a sheared granular bed containing two and three sizes of particles. Granul. Matter 14 (2), 215–220.

Yang, Z., Fan, X., Fryer, P.J., Parker, D.J., Bakalis, S., 2007. Improved multiple-particle tracking for studying flows in multiphase systems. AIChE J. 53 (8), 1941–1951.

Zhu, C., Wang, X., Fan, L.-S., 2000. Effect of solids concentration on evaporative liquid jets in gas–solid flows. Powder Technol. 111 (1–2), 78–82.